Electronic Supplementary Material (ESI) for Energy & Environmental Science.

Electronic Supplementary Information: Efficiency gains for thermally coupled solar hydrogen production in extreme cold

Moritz Kölbach,[1, 2] Kira Rehfeld,[3] and Matthias M. May[2]

[1] *Helmholtz-Zentrum Berlin für Materialien und Energie GmbH, Institute for Solar Fuels, Germany*
[2] *Universität Ulm, Institute of Theoretical Chemistry, Germany*
[3] *Ruprecht-Karls-Universität Heidelberg, Institute of Environmental Physics, Germany*

I. MATERIALS AND METHODS

A. Climate data for the global assessment of the solar water splitting benefit from thermal coupling

We used the latest version of the ERA5 reanalysis [1, 2]. To assess the energy harvesting potential for solar-water splitting, we require high-resolution information on temperature and insolation. Solar radiation output in ERA5 has been favourably evaluated globally [3] and at high latitudes [4, 5]. Surface temperature characteristics at high latitudes are also well captured [6, 7]. Climate and solar input were analysed based on global fields of surface temperature (variable 'tas') and surface downward shortwave radiation (variable 'ssrd') at daily/less than 31 km resolution. A day (defined as 24-hour period) is considered suitable for solar-water-splitting with a device if its average (24-hour) temperature is within the temperature envelope of the device. The temperature thresholds we consider are (a) above the freezing point of water (273 K) for conventional electrolysis, (b) above 253 K, the minimal temperature we have evaluated our device for, and (c) above the freezing point of 30 wt% sulphuric acid, 238 K, which can be seen as the lowest temperature limit of the device. The added solar water-splitting potential in Jm^{-2}, or the energy that we estimate could have been harvested in 2019 under the expected limitations of the proposed device, is calculated as a weighted sum $Q_\mathrm{t} = \sum_{i=1}^{365} p(t)_i q_i$, with the weight for day, i, set to unity if its mean temperature is above the temperature threshold T_0: $p_i = 1$ if $t_i \geq T_0$ and to zero if it is not, and $p_i = 0$ if $t_i < T_0$.

B. The harvesting potential of storable renewable energy for high-latitude and high-altitude research stations

We assess the opportunity for local production of renewable, storable energy at 100 high-latitude and high-altitude research stations and field camps. Location details for active stations were compiled based on publicly available information and publications [8]. Supplementary Table 5 provides coordinates, names, operators, and links as well as the estimated solar water-splitting energy harvesting potential for the year 2019. Temperature and radiation for the station locations was extracted from ERA5 reanalysis output using bilinear interpolation. Comparing the theoretical efficiency of a triple-junction solar cell for AM1.5G with the efficiency for a spectrum to be expected in Antarctica[9], we find the limit to drop by 6% relative. Therefore, we estimate a relative error for the solar hydrogen harvesting potential in Fig. 4 as 10%.

C. Device model description

1. *Thermal flux for a thermally coupled device*

In our model for the thermally coupled device design adapted from Min et al. [10], we assume that the temperature of the electrolyte is equal to the operating temperature of the solar cells, denoted as the device temperature ($\mathrm{T}_\mathrm{device}$). Ignoring heat transfer by educt and product flux, the device reaches its quasi-steady temperature when the absorbed luminous power (P_in) equals the sum of the fraction of the luminous power used to split water at thermoneutral conditions ($f \cdot P_\mathrm{in}$) plus the power dissipated by radiation (q_rad) and convection (q_conv):

$$P_\mathrm{in} - f \cdot P_\mathrm{in} - q_\mathrm{rad} - q_\mathrm{conv} := 0 \tag{1}$$

The absorbed luminous power can be described using the following equation,

$$P_\mathrm{in} = T_\text{optical-train} \cdot A_\text{solar-cells} \cdot I_0 \tag{2}$$

where $T_{\text{optical-train}}$ is the transmissivity of the optical train, $A_{\text{solar-cells}}$ is the area of the solar cells, and I_0 is the power density of the incident radiation. The fraction f of the absorbed luminous power that is used to split water at thermoneutral conditions can be expressed as

$$f{=}\frac{j_{\text{op}}\left(T_{\text{device}}\right)\cdot E_{\text{op}}\left(T_{\text{device}}\right)}{C\cdot I_0}\cdot\left(\frac{E_{\text{th}}}{E_{\text{op}}\left(T_{\text{device}}\right)}\right), \tag{3}$$

where j_{op} is the temperature-dependent operation current density, C is the light concentration factor, and E_{th} is thermoneutral voltage for water splitting of 1.48 V. Note that the influence of the temperature on E_{th} is very small and is neglected here.[11] The power dissipated through radiation can be described as follows:

$$q_{\text{rad}}{=}\sigma\cdot\left(A_{\text{solar cells}}\cdot\varepsilon_{\text{solar cells}}{+}A_{\text{housing}}\cdot\varepsilon_{\text{housing}}\right)\cdot\left({T_{\text{device}}}^4{-}{T_{\text{out}}}^4\right). \tag{4}$$

Here, σ is the Stephan-Boltzmann constant, $\varepsilon_{solarcells}$ is the surface emissivity, A_{housing} is the area of the device housing, $\varepsilon_{housing}$ is the surface emissivity of the housing, and T_{out} is the outdoor temperature. The power dissipated through convection can be expressed as

$$q_{\text{conv}}{=}\left(A_{\text{solar cells}}\cdot h_{\text{solar cells - air}}\cdot{+}A_{\text{housing}}\cdot U_{\text{t}}\right)\cdot\left(T_{\text{device}}{-}T_{\text{out}}\right), \tag{5}$$

where $h_{\text{solar cells - air}}$ is the convective transfer coefficient, and U_{t} is the overall heat transfer coefficient. The latter can be used to implement effects of insulation with a thickness of l_{ins} and a thermal conductivity k_{ins} around the device housing and is given by:

$$U_{\text{t}}{=}\frac{1}{\frac{l_{\text{ins}}}{k_{\text{ins}}}+\frac{1}{h_{\text{housing - air}}}} \tag{6}$$

2. *Thermal flux for a decoupled device*

For the decoupled device design, we estimate the operating temperature of the solar cell by assuming that an area of twice the solar cell area is available for heat dissipation and that the electrolyte temperature is equal to the outdoor temperature. This implies that the sun and the operating potential E_{op} higher than the thermoneutral voltage do not heat up the electrolyte. The fraction $f_{\text{decoupled}}$ of the absorbed luminous power that is used to split water can then be expressed as:

$$f_{\text{decoupled}}{=}\frac{j_{\text{op}}\left(T_{\text{device}}\right)\cdot E_{\text{op}}\left(T_{\text{device}}\right)}{C\cdot I_0} \tag{7}$$

3. *Electrochemistry*

The following part describes the temperature-dependent IV-characteristics for a 2-electrode water splitting setup based on the single OER and HER catalyst characteristics in an aqueous electrolyte. The temperature-dependent standard potential of the OER is given by:

$$E_{0,\text{ OER}}\left(T_{\text{device}}\right)=E_{0,\text{OER, T}_{\text{ref}}}{+}\left(T_{\text{device}}{-}T_{\text{ref}}\right)\cdot E_{0,\text{OER, T}_{\text{coeff}}} \tag{8}$$

Here, $E_{0,\text{OER}, T_{\text{ref}}}$ is the standard potential at the reference temperature T_{ref}, and $E_{0,\text{OER}, T_{\text{coeff}}}$ is the temperature coefficient. By definition, the standard potential of the HER is zero:

$$E_{0,\text{ HER}}\left(T_{\text{device}}\right)=0 \tag{9}$$

The Nernst-potentials of the OER and HER can be expressed as follows:

$$E_{\text{OER, Nernst}}\left(T_{\text{device}}\right)=E_{0,\text{ OER}}\left(T_{\text{device}}\right)-\frac{R\cdot T_{\text{device}}}{z\cdot F}\cdot 2.303\cdot z\cdot pH \tag{10}$$

$$E_{\text{HER, Nernst}}\left(T_{\text{device}}\right) = E_{0,\text{ HER}}\left(T_{\text{device}}\right) - \frac{R \cdot T_{\text{device}}}{z \cdot F} \cdot 2.303 \cdot z \cdot pH, \tag{11}$$

where z is the number of electrons involved in the reaction, F is the Faraday constant, R is the universal gas constant, and pH is the pH value of the aqueous electrolyte. The thermodynamic potential of the water splitting reaction is then defined as the difference between the Nernst-potential of the HER and OER:

$$E_{\text{redox}}\left(T_{\text{device}}\right) = E_{\text{HER, Nernst}}\left(T_{\text{device}}\right) - E_{\text{OER, Nernst}}\left(T_{\text{device}}\right) \tag{12}$$

The OER current as a function of the applied potential E can be modelled using the anodic branch of the Butler-Volmer equation:

$$j_{OER}\left(E, T_{\text{device}}\right) = j_{0,OER}\left(T_{\text{device}}\right) \cdot \left[\exp\left(\frac{\alpha_{\text{a, OER}} \cdot z \cdot F \cdot \left(E - E_{\text{OER, Nernst}}\left(T_{\text{device}}\right)\right)}{R \cdot T_{\text{device}}}\right)\right], \tag{13}$$

where $\alpha_a \cdot z$ is the anodic charge transfer coefficient multiplied with the number of electrons involved that can be extracted from the tafel slope, and $j_{0,\text{OER}}$ is the temperature-dependent exchange current density, which can be calculated from the exchange current density $j_{0,\text{OER, T}_{\text{ref}}}$ at the reference temperature T_{ref} and the activation energy $E_{\text{a,OER}}$ as follows:

$$j_{0,\text{OER}}\left(T_{\text{device}}\right) = j_{0,\text{OER, T}_{\text{ref}}} \cdot \exp\left[\frac{E_{\text{a,OER}}}{R} \cdot \left(\frac{1}{T_{\text{ref}}} - \frac{1}{T_{\text{device}}}\right)\right] \tag{14}$$

Note that mass transport limitations are neglected in this model for simplicity. The HER current as a function of the applied potential can be modelled analogously:

$$j_{\text{HER}}\left(T_{\text{device}}\right) = j_{0,\text{HER}}\left(T\right) \cdot \left[-\exp\left(\frac{-\alpha_{\text{c, HER}} \cdot z \cdot F \cdot \left(E - E_{\text{HER, Nernst}}\left(T_{\text{device}}\right)\right)}{R \cdot T_{\text{device}}}\right)\right] \tag{15}$$

$$j_{0,\text{HER}}\left(T_{\text{device}}\right) = j_{0,\text{HER, T}_{\text{ref}}} \cdot \exp\left[\frac{E_{\text{a,HER}}}{R} \cdot \left(\frac{1}{T_{\text{ref}}} - \frac{1}{T_{\text{device}}}\right)\right] \tag{16}$$

In the model, the OER and HER current are merged to the (ohmic loss-free) 2-electrode overall water splitting current $\text{j}_{\text{catalysts}}(E, T_{\text{device}})$. Subsequently, the ohmic loss is calculated from the distance of the electrodes d, the geometry correction factor G_{corr} and the temperature-dependent conductivity of the aqueous electrolyte $\kappa_{\text{electrolyte}}$ as follows:

$$iR_{\text{loss}}\left(E, T_{\text{device}}\right) = \frac{j_{\text{catalysts}}\left(E, T_{\text{device}}\right) \cdot d}{G_{\text{corr}} \cdot \kappa_{\text{electrolyte}}\left(T_{\text{device}}\right)} \tag{17}$$

The linear correlation of the electrolyte conductivity with temperature is given by:

$$\kappa_{\text{electrolyte}}\left(T_{\text{device}}\right) = y_0 + m \cdot T_{\text{device}} \tag{18}$$

4. Solar cell

Our model can perform the calculation of the temperature-dependent solar cell IV-characteristics using the detailed balance limit or experimental parameters from the manufacturer's datasheet[12]. Here we used the latter. The temperature and intensity dependence of the short-circuit current density I_{sc}, the open circuit potential V_{oc} can be approximated as:

$$I_{\text{sc}}\left(T_{\text{device}}\right) = I_{\text{sc, T}_{\text{ref}}} + T_{\text{coeff, I}_{\text{sh}}} \cdot \left(T_{\text{device}} - T_{\text{ref, sh}}\right) \cdot I_{\text{sc, T}_{\text{ref}}} \tag{19}$$

$$V_{\text{oc}}\left(T_{\text{device}}\right) = V_{\text{oc, T}_{\text{ref}}} + T_{\text{coeff, V}_{\text{oc}}} \cdot \left(T_{\text{device}} - T_{\text{ref}}\right) \cdot V_{\text{oc, T}_{\text{ref}}} \tag{20}$$

$$I_{\text{sc}}\left(T_{\text{device}}, C\right) = I_{\text{sc}}\left(T_{\text{device}}\right) \cdot C \tag{21}$$

$$V_{\text{oc}}\left(T_{\text{device}}, C\right) = V_{\text{oc}}\left(T_{\text{device}}\right) + n_{\text{i}} \cdot E_{\text{T}} \cdot \ln\left(C\right) \tag{22}$$

where $I_{\mathrm{sc},\,T_{\mathrm{ref}}}$ is the short-circuit current density at the reference temperature T_{ref}, $T_{\mathrm{coeff,\,I_{sh}}}$ is the temperature coefficient of the short-circuit current density, $V_{\mathrm{oc},\,T_{\mathrm{ref}}}$ is the open circuit potential at the reference temperature T_{ref}, $T_{\mathrm{coeff,\,V_{oc}}}$ is the temperature coefficient of the open circuit potential. The inclusion of experimental temperature coefficients of both V_{oc} and I_{sc} implies that also the typical (blue-) shifts of bandgaps with decreasing temperatures, leading to a change in the absorption threshold, are fully captured. The thermal voltage E_{T} is defined as $k_b T/e$, where k_b is the Boltzmann constant k_b and e is the electron charge. Note that for calculations employing low light concentration, the influence of the concentration on $T_{\mathrm{coeff,\,V_{oc}}}$[13] is neglected. Using the single diode equation and neglecting the influence of shunt and series resistances, the temperature-dependent IV-characteristics of the solar cell can be approximated by [14]:

$$j_{\text{solar cells}}\left(T_{\text{device}},E\right)=j_{\text{sh}}\left(T_{\text{device}}\right)\cdot\left[1-\frac{\exp\left[\left(\frac{E}{n_{\mathrm{i}}\cdot E_{\mathrm{T}}}\right)-1\right]}{\exp\left[\left(\frac{V_{\mathrm{oc}}\left(T_{\text{device}}\right)}{n_{\mathrm{i}}\cdot E_{\mathrm{T}}}\right)-1\right]}\right] \tag{23}$$

5. STH efficiency

To obtain the operating current density j_{op}, the model matches the IV-characteristics of the solar cell and the 2-electrode catalyst current for overall water splitting based on the $A_{\text{catalyst}}/\ A_{\text{solar cells}}$-ratio:

$$j_{\text{catalysts}}\left(T_{\text{device}},E\right)=j_{\text{solar cells}}\left(T_{\text{device}},E\right):=j_{\text{op}}\left(T_{\text{device}}\right) \tag{24}$$

Since the device temperature depends on the operating current density (and vice versa, see equation 3), our model iteratively solves equations 1 to 24 until convergence is reached. Finally, the STH efficiency is calculated as follows, assuming a Faradaic efficiency of unity:

$$STH=\left[\frac{j_{\text{op}}\left(T_{\text{device}}\right)\cdot E_{\text{redox}}\left(T_{\text{device}}\right)}{C\cdot I_{0}}\right] \tag{25}$$

We assume $E_{\mathrm{redox}} = 1.23\,\mathrm{eV}$, corresponding to consumption in a fuel cell by at room temperature. For the generation, on the other hand, we take into account its temperature-dependence, $E_{\mathrm{redox}}(T)$. If not otherwise stated, the input parameters listed in SI Table 1,2,3 and 4 are used.

D. Device design

15 GaInP/GaInAs/Ge solar cells (CPV 3C44, Azur Space) with an photoactive size of 10 x 10 mm^2 were back-contacted on a 55 x 40 mm^2 polished copper sheet with a thickness of 0.35 mm using electrically conductive epoxy adhesive (Elecolit 323, Panacol) with the help of a laser-cut placing mask. The front contacts were connected in parallel by wire bonding. The copper plate was attached to a macro-cuvette (402.000-OG, Hellma Analytics) with a thin thermally conductive double-sided adhesive foil (WLFT 404, Fischer Elektronik) to ensure good thermal coupling. The outer dimensions of the cuvette were 55 x 40 x 23.6 mm^3 with a wall thickness of 2 mm. A 5 x 55 mm^2 black polyvinyl sheet was used to mask the busbar for the front-contact resulting in a total illuminated area of 19.25 cm^2. The positive and negative terminal of the solar cell array was wired to the OER-catalyst ($\mathrm{IrO_x}$ on a titanium mesh with 12 g Ir/m^2, Metakem) and HER-catalyst (platinised titanium mesh with 50 g Pt/m^2, Metakem), respectively. Both catalysts were 3.0 x 1.0 cm^2, which translates into a surface area of 5.1 cm^2 when accounting for the surface factor of 1.7 of the mesh. The catalysts were positioned parallel to each other separated by 1 cm. A PTFE wedge in parallel to the catalysts at a separation of 0.75 cm to the cuvette bottom was used for product separation. The distance between the lower edge of the catalysts and the cuvette bottom was 1.9 cm. The cuvette was filled with 22 ml of 30 wt% H_2SO_4 (pure, Carl Roth) as an electrolyte. For experiments with insulation, the cell was covered in aluminium foil (emissivity of 0.2) and inserted into a 2 cm thick foamed polystyrene housing (thermal conductivity of 0.03 Wm^{-1}K^{-1}). Photographs of the cell are shown in SI Figure 6.

E. Device characterisation

To perform experiments at low temperatures, the device was put into a freezer (LGUex1500, Liebherr) and illuminated through an 8 x 8 cm^2 hole in the door that was covered with a 0.5 cm thick quartz plate. As an illumination source, a

WACOM Class AAA solar simulator (WXS-100S-L2H, AM1.5G, 1000 W/m^2) was used. The overall power, as measured within the fridge, was set to 1000 W/m^2 using a S401C powermeter (Thorlabs). Such a single-point calibration for a multi-junction cell is, in principle, prone to errors due to the spectral mismatch between solar simulator and the AM1.5G standard spectrum. In our case of an almost perfectly current-matched triple junction, this does, however, not lead to an over- but rather an underestimation of the overall efficiency, as follows. Optimising the power ratio of the xenon and halogen lamps while keeping the total power at 1000 W/m^2, resulted in a current density of 13.15 instead of the 15.4 as reported in the datasheet. Raising the current to the photocurrent from the datasheet of a reference cell without correcting the total power by an infrared filter, as is sometimes done in the literature [15], might artificially increase the overall efficiency due to higher thermal power available for heating the electrolyte, and is therefore avoided here. The quartz plate (without anti-reflection coating) as our optical train was inserted into the light path after light-power calibration. For the efficiency calculation, the total illuminated area of 19.25 cm^2 instead of the 15 cm^2 photoactive area was used. These effects mean that the measured efficiencies are conservative values. The temperature of the electrolyte during the experiments was monitored with a PT1000 sensor encapsulated in epoxy resin (832HD, MG Chemicals). The reference temperature in the freezer was measured with a PT1000 sensor which was located behind the cell. The control loop of the freezer resulted in mean freezer temperatures between -19.2 °C and -20.5 °C (see SI Fig. 7) during the measurements under AM1.5G illumination. For the electrochemical characterisation, an Amel potentiostat-galvanostat (model 2551) equipped with an Amel frequency response analyser (model 2700) were used. The IV curves were measured in a 2-electrode configuration with a scan rate of 10 mV/s. The operating current for unassisted water splitting and the operation voltage between the HER- and OER-catalyst were measured with two Keysight 34461A digital multimeters. The resistance of the multimeter of 0.5 Ω for the operation current measurement was used to correct the IV curves of the catalysts in thermal equilibrium shown in Fig. 3c. During operation, no measures were taken to remove the gas bubbles. IV curves of the solar cell array were recorded using a Keysight 2400 source meter with a scan rate of 100 mV/s. For reference measurements in the thermally non-coupled device configuration, the solar cell array on the empty cuvette was illuminated, while the electrochemical compartment was placed in a second cuvette in the freezer located out of the direct beam path.

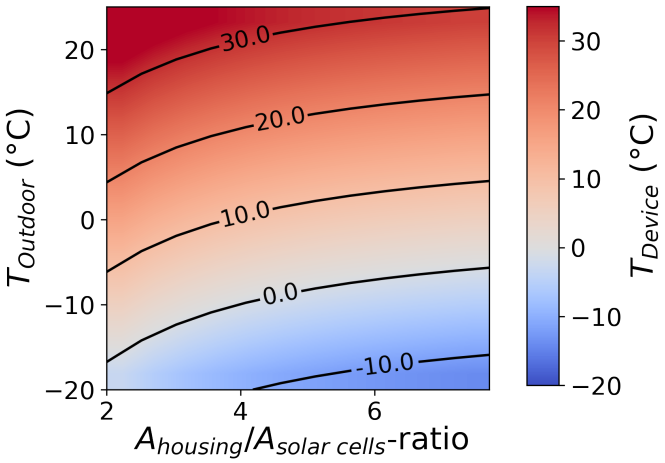

Figure S 1. **Influence of the $\mathbf{A_{housing}/A_{solar\text{-}cells}}$-ratio on the device temperature.** Equilibrium temperature of a thermally coupled device based on a double junction as a function of the outdoor temperature and the $A_{housing}/A_{solar\text{-}cells}$-ratio from the extended YaSoFo[12] model.

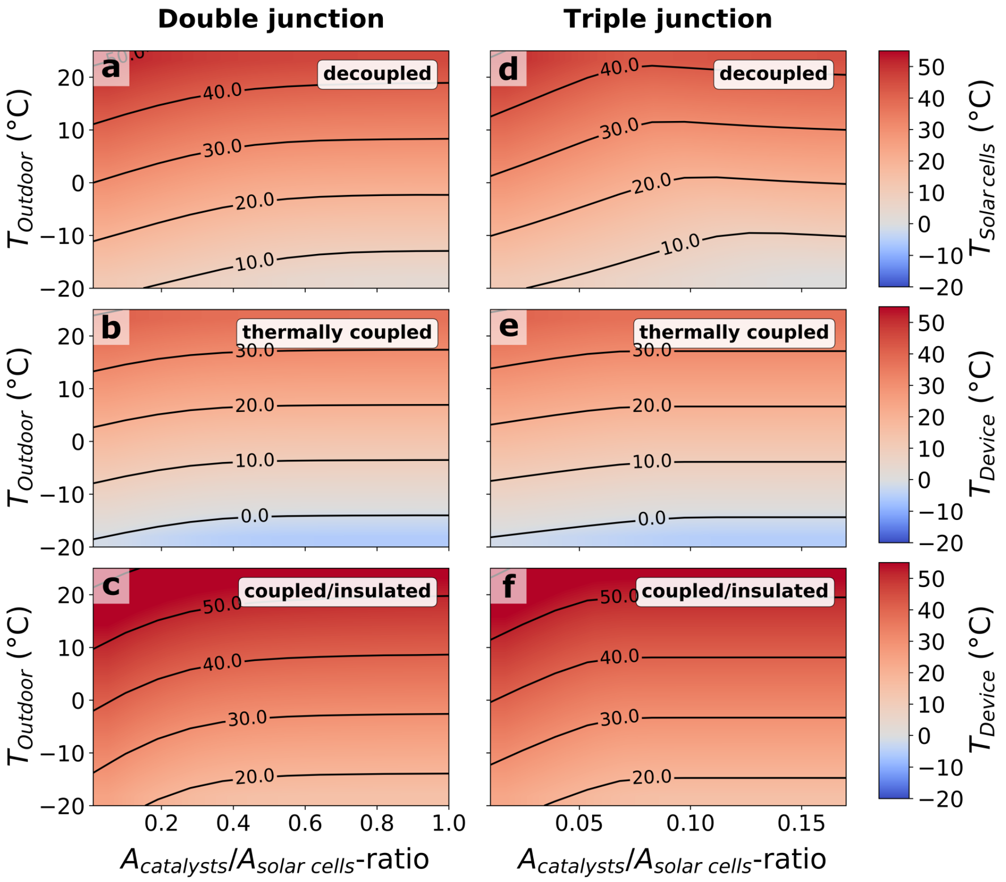

Figure S 2. **Comparison of temperatures and device aspect ratio for double junction and triple junction solar cells.** Solar cell (**a**,**d**) and device temperatures (**b**,**c**,**e**,**f**) corresponding to Fig. 2c-h in the main manuscript.

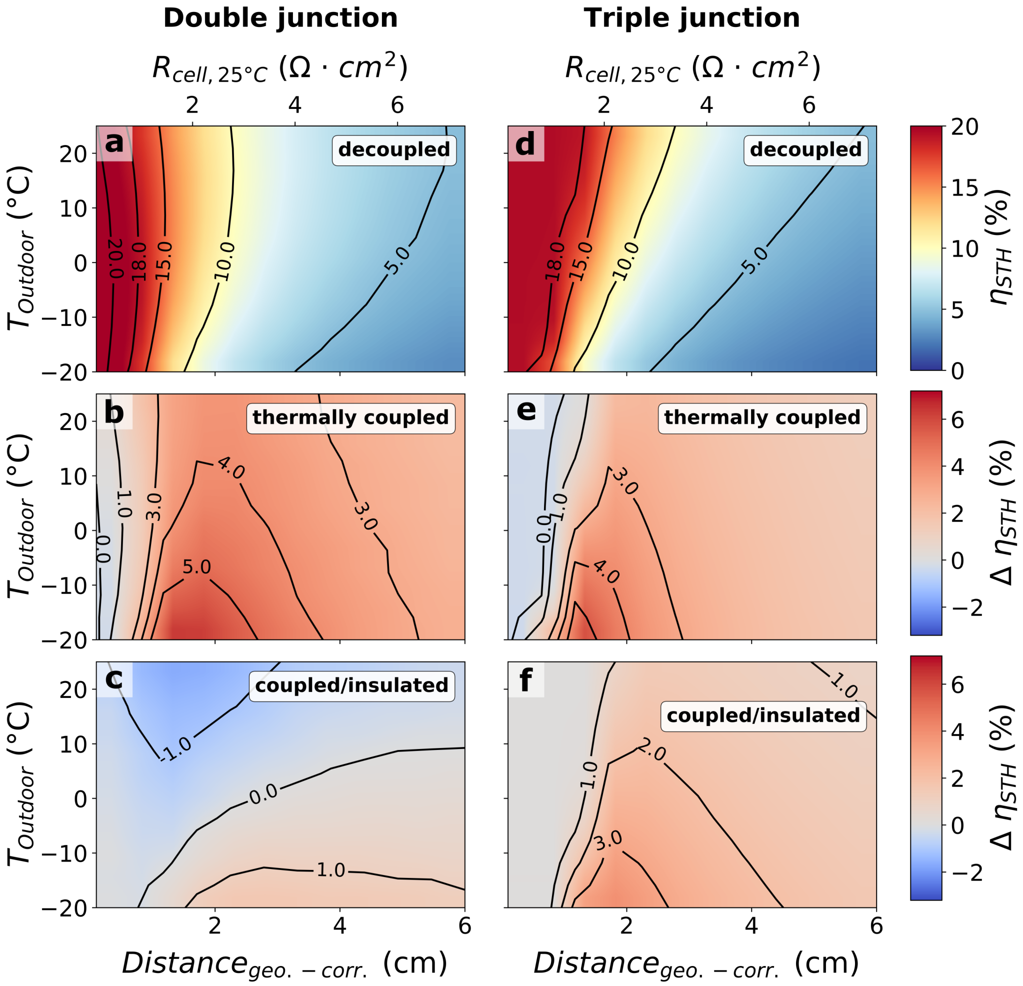

Figure S 3. **Comparison of efficiencies and thermal requirements of double- and triple-junction solar cells. a-f)** Modelled STH efficiencies and efficiency gains as a function of the geometry corrected distance of the electrodes for the decoupled, thermally coupled, and coupled as well as insulated case using a double junction **(a,b,c)** and a triple junction **(d,e,f)** solar cell. **b,e)**: Increase in absolute STH efficiency caused by thermal coupling in comparison to the non-coupled device. **c,f)**: Efficiency gain from insulation of the electrochemical compartment referring to the coupled configuration. The upper x-axis indicates the cell resistance at T = 25 °C.

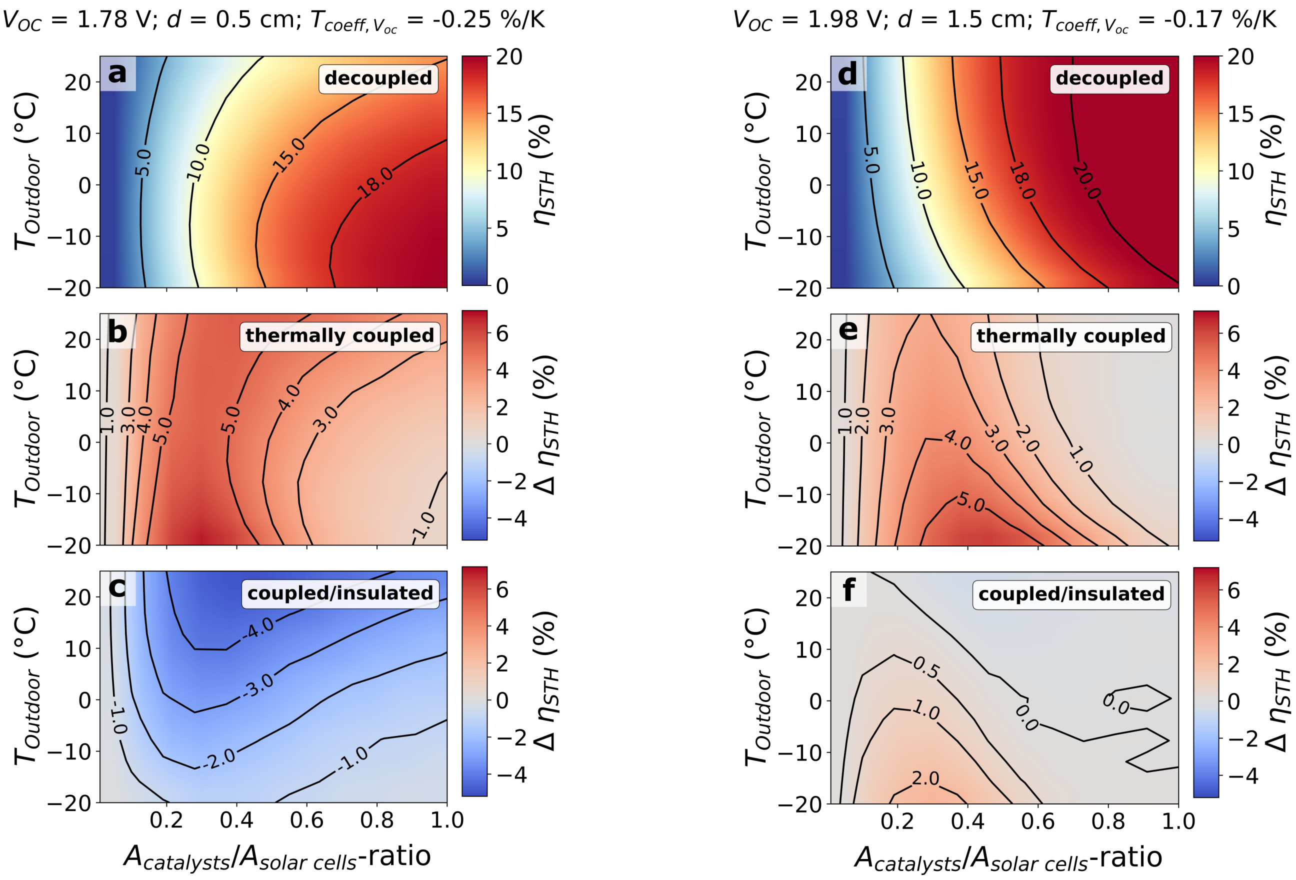

Figure S 4. **Modelled STH efficiencies and efficiency gains as a function of the $A_{catalyst}/A_{solar\ cells}$-ratio for the decoupled, thermally coupled, and coupled as well as insulated case using a double junction. b,e)**: Increase in absolute STH efficiency caused by thermal coupling in comparison to the non-coupled device. **c,f)**: Efficiency gain from insulation of the electrochemical compartment referring to the coupled configuration. Two sets of calculations are shown with a slightly changed open circuit potential (± 0.1 V), temperature coefficient of the open circuit potential (± 0.04 %/K), and the distance (± 0.5 cm) with respect to the input parameters of Fig. 2c-d. **a,b,c)**: STH efficiencies do not significantly drop with decreasing temperature. Hence, the insulation of the electrochemical compartment is detrimental. **d,e,f)**: STH efficiencies continuously drop with decreasing temperature resulting in a solely beneficial effect of the insulation.

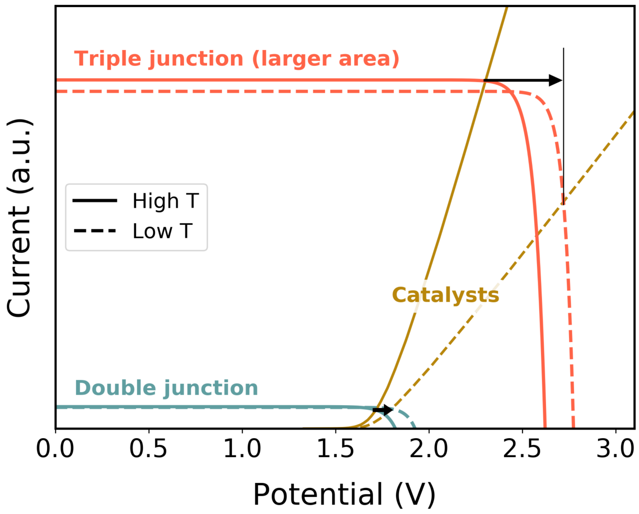

Figure S 5. **Qualitative comparison of the influence of cold temperatures on the IV characteristics of devices based on double and triple junction solar cells operating near the maximum power point.** Solid and dashed lines represent the high and low temperature case, respectively. To ensure an operation near the maximum power point in the high temperature case, the triple junction solar cell has a larger area, i.e. a lower $A_{catalyst}/A_{solar\ cells}$-ratio. Therefore, the catalysts operates at a higher current density which translates into a higher voltage losses with decreasing temperature due to the ohmic-like behaviour as indicated with the black arrows.

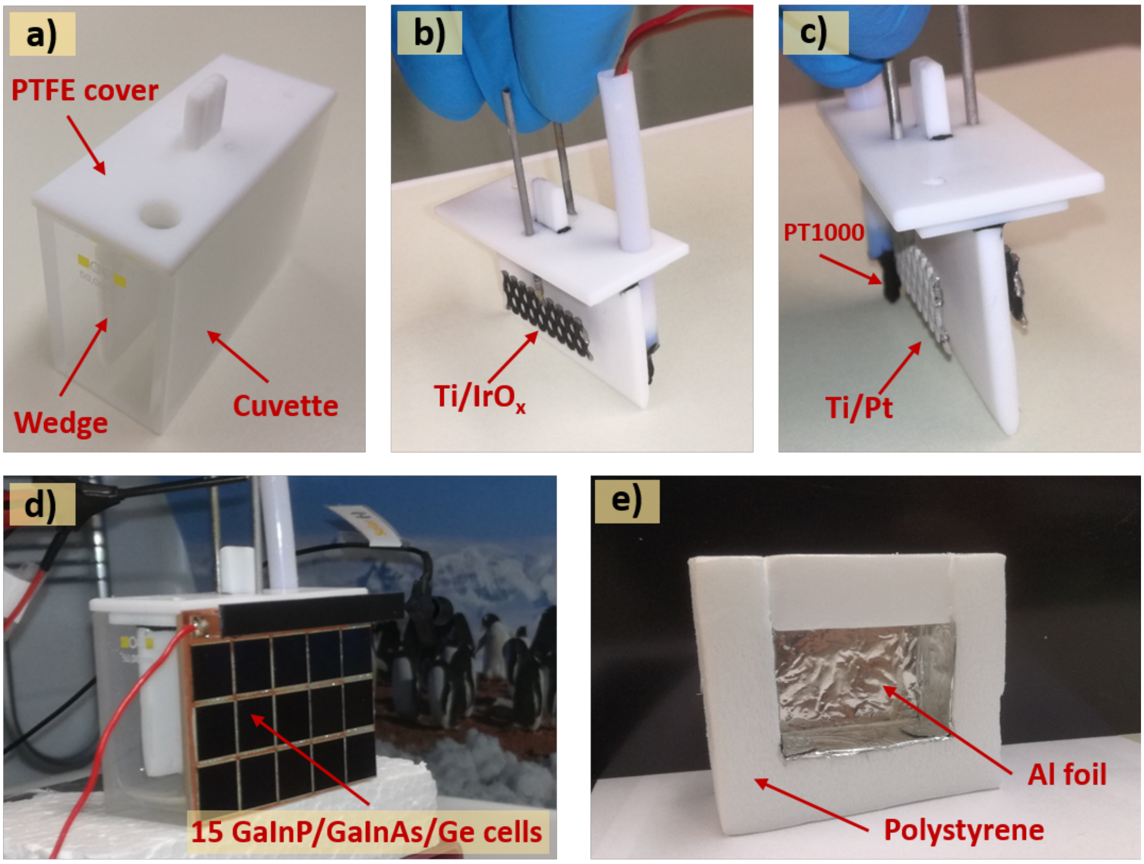

Figure S 6. **Details of the experimental setup.a)** Cuvette with PTFE cover and wedge. **b,c)** PTFE cover and wedge with mounted Pt- and IrO$_x$-catalysts and epoxy-encapsulated PT1000 sensor. **d)** Cuvette with solar-cell array attached in the freezer. **e)** Insulation made of closed-cell extruded polystyrene foam and aluminium foil.

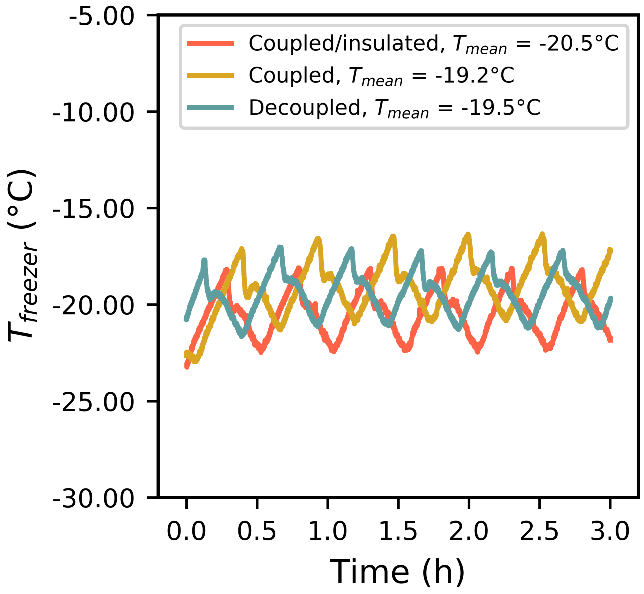

Figure S 7. **Environmental temperature during experiments.** The air temperature in the freezer was measured with a PT1000 sensor behind the water-splitting device (i.e. shadowed by the device, no direct irradiation) during the measurements shown in Fig. 3b-d.

Supplementary note 1: Fig. 8 and Fig. 9 show the influence of low light concentration on the calculations shown in Fig. 2 in the manuscript. Both figures again emphasise the beneficial effect of thermal coupling and that an insulation helps when the device suffers from low temperatures. Moreover, it can be seen that low light concentration would shift the cost from the absorber to the catalyst and optics since higher $A_{catalyst}/A_{solar\ cells}$-ratios are needed to ensure operation below the MPP. Note that especially for the insulated design, device temperatures of above 100 °C are reached for $C > 2$. Here, extra heat sinks or active cooling (e.g. flowing electrolyte) would have to be employed.

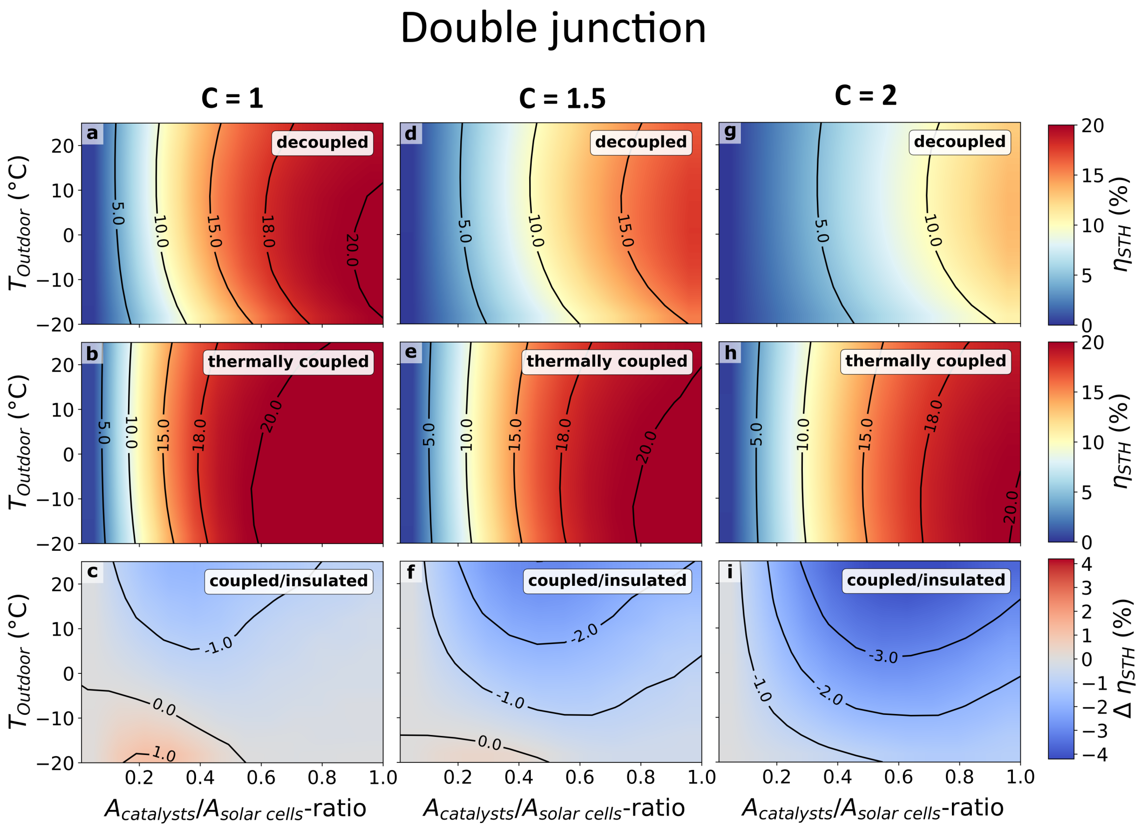

Figure S 8. **Modelled STH efficiencies and efficiency gains using light concentration as a function of the $A_{catalyst}/A_{solar\ cells}$-ratio for the decoupled, thermally coupled, and coupled as well as insulated case using a double junction. a,b,c)**: Reference calculations for $C = 1$ showing the STH efficiency for the decoupled and thermally coupled configuration, as well as the efficiency gain/losses from insulation of the electrochemical compartment referring to the coupled configuration. **d,e,f)** and **g,h,i)** show the same plots for $C = 1.5$ and $C = 2$, respectively.

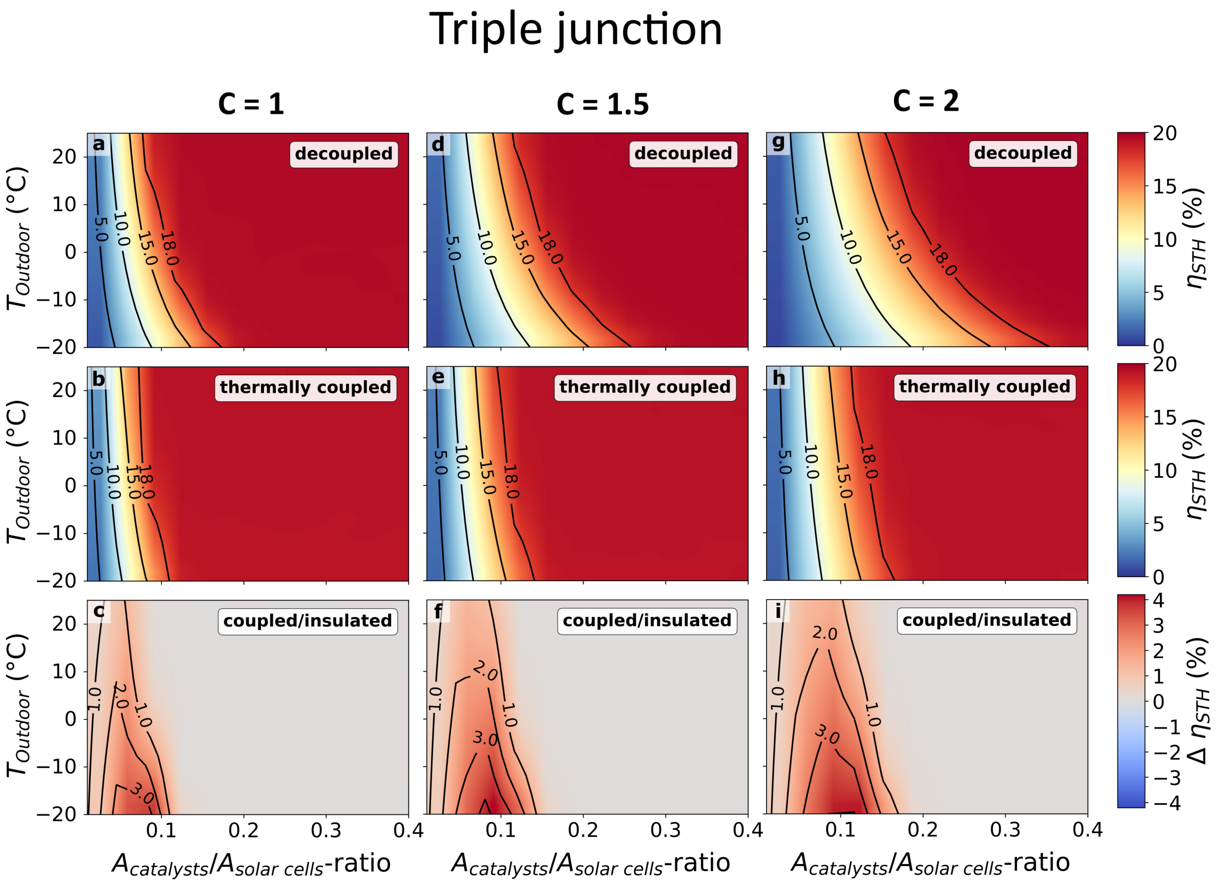

Figure S 9. **Modelled STH efficiencies and efficiency gains using light concentration as a function of the $A_{catalyst}/A_{solar\ cells}$-ratio for the decoupled, thermally coupled, and coupled as well as insulated case using a triple junction. a,b,c)**: Reference calculations for C = 1 showing the STH efficiency for the decoupled and thermally coupled configuration, as well as the efficiency gain/losses from insulation of the electrochemical compartment referring to the coupled configuration. **d,e,f)** and **g,h,i)** show the same plots for C = 1.5 and C = 2, respectively.

Table S I. Thermal model input parameters

Parameter	**Definiton**	**Values**	**Refs**
$T_{\text{optical train}}$	Transmissivity of the optical train	0.9	-
$A_{\text{housing}}/A_{\text{solar cell}}$	Area ratio of the device housing and the solar cells	2.5	-
I_0	Irradiance of the incident light	$1000\,\text{W/m}^2$	-
$\varepsilon_{\text{solar cells}}$	Emissivity of the solar cells	0.9	-
$\varepsilon_{\text{housing}}$	Emissivity of the device housing	0.9	-
$h_{\text{solar cells - air}}$	Convective transfer coefficient solar cells - air	$10\,\text{W/(m}^2\text{K)}$	-
$h_{\text{housing - air}}$	Convective transfer coefficient device housing - air	$10\,\text{W/(m}^2\text{K)}$	-
l_{ins}	Thickness of the insulation	2 cm	-
κ_{ins}	Thermal conductivity of the insulation	0.03 W/(m K)	-

Table S II. Catalyst model input parameters

$j_{0,\text{ OER, T}_{\text{ref}}}$	OER exchange current density	$1.86 \times 10^{-9}\,\text{A/cm}^2$ for IrO_x at $T_{\text{ref}} = 323\,\text{K}$	[16]
$E_{\text{a, OER}}$	Activation Energy OER	52 kJ/mol	[16]
$\alpha_{\text{a,OER}} \cdot z$	Anodic charge transfer coefficient of the OER multiplied with the electrons involved (can be extracted from the Tafel slope)	1.5	[16]
$j_{0,\text{ HER, T}_{\text{ref}}}$	HER exchange current density	$0.68 \times 10^{-3}\,\text{A/cm}^2$ for Pt at $T_{\text{ref}} = 303\,\text{K}$	[17]
$E_{\text{a, HER}}$	Activation Energy HER	13.2 kJ/mol	[17]
$\alpha_{\text{c, HER}} \cdot z$	Cathodic charge transfer coefficient of the HER multiplied with the electrons involved (can be extracted from the Tafel slope)	1.2	[17]

Table S III. Solar cell model input parameters

$I_{\text{sc, double}}$	Short current density of a double-junction solar cell	$17.0\,\text{mA/cm}^2$ at $T_{\text{ref}} = 298.15\,\text{K}$	-
$I_{\text{sc, triple}}$	Short current density of a triple-junction solar cell	$15.6\,\text{mA/cm}^2$ at $T_{\text{ref}} = 298.15\,\text{K}$	Azur Space data sheet
$T_{\text{coeff, I}_{\text{sh, double}}}$	Short current density temperature coefficient of a double junction solar cell	0.08 %/K	-
$T_{\text{coeff, I}_{\text{sh, triple}}}$	Short current density temperature coefficient of a triple junction solar cell	0.08 %/K	Azur Space data sheet
$V_{\text{oc, double}}$	Open circuit potential of a double junction solar cell	1.88 V at $T_{\text{ref}} = 298.15\,\text{K}$	-
$V_{\text{oc, triple}}$	Open circuit potential of a triple junction solar cell	2.7 V at $T_{\text{ref}} = 298.15\,\text{K}$	Azur Space data sheet
$T_{\text{coeff, V}_{\text{oc, double}}}$	Open circuit potential temperature coefficient of a double junction solar cell	-0.21 %/K	-
$T_{\text{coeff, V}_{\text{oc, triple}}}$	Open circuit potential temperature coefficient of a triple junction solar cell	-0.135 %/K	Azur Space data sheet
n_{i}	Diode ideality factor	2	Azur Space data sheet

Table S IV. Device configuration model input parameters

pH	pH value of the electrolyte	0	-
y_0, m	Linear parameters of the electrolyte conductivity according to $\kappa_{electrolyte}=y_0+m\cdot T$ in [S/cm]	y_0 = -2.686 m = 0.01176	[18]
$A_{\text{housing}}/A_{\text{solar cells}}$	Ratio of the device housing and the solar cell area	2.5	-
$A_{\text{catalyst}}/A_{\text{solar cells}}$ (double junction)	Ratio of the catalysts and the solar cell area of the device based on a double junction	0.5	-
$A_{\text{catalyst}}/A_{\text{solar cells}}$ (triple junction)	Ratio of the catalysts and the solar cell area of the device based on a triple junction	0.1	-
d	Distance of the electrodes	1 cm	-
G_{corr}	Geometry correction factor: ratio of the resistance of a restricted cell[19] with no obstacle in between the electrodes (e.g. wedge for product separation) and the real cell resistance during operation	0.3	-

REFERENCES

[1] H. Hersbach, B. Bell, P. Berrisford and S. Hirahara, *Quarterly Journal of the Royal Meteorological Society*, 2020, **146**, 1999–2049.

[2] H. Hersbach, B. Bell, P. Berrisford, G. Biavatti, A. Horányi, J. Muñoz Sabater, J. Nicolas, , C. Peubey, R. Radu, I. Rozum, D. Schepers, A. Simmons, C. Soci, D. Dee and J.-N. Thépaut, *ERA5 hourly data on single levels from 1979 to present*, Copernicus Climate Change Service (C3S) Climate Data Store (CDS), 2018, `https://doi.org/10.24381/cds.adbb2d47`, (Accessed on < 28-12-2020 >).

[3] D. Yang and J. M. Bright, *Solar Energy*, 2020, **210**, 3–19.

[4] B. Babar, R. Graversen and T. Boström, *Solar Energy*, 2019, **182**, 397–411.

[5] M. Seo, H. C. Kim, K. S. Lee, N. H. Seong, E. Lee, J. Kim and K. S. Han, *Journal of Sensors*, 2020, **2020**, 8825870.

[6] D. Tetzner, E. Thomas and C. Allen, *Geosciences*, 2019, **9**, 289.

[7] A. Delhasse, C. Kittel, C. Amory, S. Hofer, D. Van As, R. S. Fausto and X. Fettweis, *The Cryosphere*, 2020, **14**, 957–965.

[8] M. V. Madsen, H. C. Steen-Larsen, M. Hörhold, J. Box, S. M. Berben, E. Capron, A. K. Faber, A. Hubbard, M. F. Jensen, T. R. Jones, S. Kipfstuhl, I. Koldtoft, H. R. Pillar, B. H. Vaughn, D. Vladimirova and D. Dahl-Jensen, *Journal of Geophysical Research: Atmospheres*, 2019, **124**, 2932–2945.

[9] A. R. D. Smedley, G. W. Evatt, A. Mallinson and E. Harvey, *The Cryosphere*, 2020, **14**, 789–809.

[10] C. Min, C. Nuofu, Y. Xiaoli, W. Yu, B. Yiming and Z. Xingwang, *Journal of Semiconductors*, 2009, **30**, 044011.

[11] M. Mori, T. Mržljak, B. Drobnič and M. Sekavčnik, *Strojniški vestnik - Journal of Mechanical Engineering*, 2013, **59**, 585–594.

[12] M. M. May and M. Kölbach, *YaSoFo - Yet Another SOlar Fuels Optimizer*, 2021, `https://doi.org/10.5281/zenodo.1489157`, Key reference.

[13] G. Siefer and A. W. Bett, *Progress in Photovoltaics: Research and Applications*, 2014, **22**, 515–524.

[14] Létay, G. and Bett, A. W., *Proceedings of the 17th European Photovoltaic Solar Energy Conference*, 2001, 178–181.

[15] S. Tembhurne, F. Nandjou and S. Haussener, *Nature Energy*, 2019, **4**, 399—-407.

[16] P. Lettenmeier, L. Wang, U. Golla-Schindler, P. Gazdzicki, N. A. Cañas, M. Handl, R. Hiesgen, S. S. Hosseiny, A. S. Gago and K. A. Friedrich, *Angewandte Chemie International Edition*, 2016, **55**, 742–746.

[17] N. M. Marković, B. N. Grgur and P. N. Ross, *The Journal of Physical Chemistry B*, 1997, **101**, 5405–5413.

[18] G. W. Vinal and D. Craig, *Journal of research of the National Bureau of Standards*, 1934, **13**, 689.

[19] I. Y. Ahmet, Y. Ma, J.-W. Jang, T. Henschel, B. Stannowski, T. Lopes, A. Vilanova, A. Mendes, F. Abdi and R. van de Krol, *Sustainable Energy Fuels*, 2019, **3**, 2366–2379.